RESEARCH ARTICLE

NANO · MICRO small
www.small-journal.com

Mediated by Polymer Intercalation Differential: Molecule Steric Hindrance Triggers 1T-2H MoS_2 Heterostructures for Ultrafast and Ultrastable Li^+/Na^+ Storage

Chen Huang, Tian Xu, Xuebin Yu, Junye Zhang, Qiuya Wang, Le Xu,* Lili Zhang, Jie Yang, Linlin Wang,* and Luyang Chen**

The organic molecule of phytic acid is innovatively utilized to block the edges of partial MoS_2 with steric effect to achieve differential intercalation of polypyrrole. After annealing, the intercalated MoS_2 nanosheet retains the 1T phase with a large spacing of 0.98 nm, while the unintercalated regions transform into the 2H phase with a small spacing (0.62 nm), thus forming a 1T-2H MoS_2 heterostructure. This structure integrates the high electrochemical activity of the 1T phase with the excellent stability of the 2H phase. Furthermore, MoS_2 nanosheets are anchored by nitrogen-doped carbon (NC) nanotubes and coated with a N/P co-doped carbon (NPC) protective layer, forming a unique sandwich hierarchical structure (NC@T/H–MoS_2@NPC). The synergistic effect of the 1T-2H MoS_2 heterostructure and the unique hierarchical structure enhances ion diffusion kinetics and structural integrity. This electrode demonstrates remarkable cycling life, with 8 000 cycles at 10 A g^{-1} in Li-ion batteries and 15 000 cycles at 5 A g^{-1} in Na-ion batteries. The 1T and 2H phases exhibit different storage Na^+/Li^+ behaviors under ex situ X-ray diffraction tests. The density functional theory results reveal the heterostructure and NC layer modulate the Fermi level, reducing Li^+/Na^+ migration energy barrier and optimizing energy storage.

1. Introduction

As the leading secondary batteries, lithium-ion batteries (LIB) and sodium-ion batteries (SIB) are widely used in various fields such as automobiles, electronic equipment, and industry for their high energy density,[1,2] which are indispensable energy storage devices in today's society. However, as application scenarios continue to expand, higher requirements are being placed on the fast charging/discharging capabilities and high cycling stability of batteries, which undoubtedly pose new challenges to the performance of electrode materials. Traditional graphite anodes, although possessing excellent cycling stability, are increasingly showing limitations in capacity and rate performance under high current densities, making it difficult to meet the growing demands. Therefore, exploring novel anode materials to break through existing bottlenecks has become a current research hotspot and key area.

Molybdenum disulfide (MoS_2) is a graphite-like material with a unique 2D layered structure, which is highly anticipated in the field of energy storage.[3] According to the coordination difference between Mo and S, the common structures of MoS_2 include rhombohedral phase (2H) and octahedral phase (1T).[4] Between them, the 2H phase MoS_2 has a small interlayer spacing (≈0.62 nm) for stable structure, and exhibits semiconductor properties with poor conductivity due to the presence of a 1.9 eV bandgap.[5,6] The 1T phase MoS_2 has metallic properties and an extended interlayer

C. Huang, J. Zhang, Q. Wang, J. Yang, L. Chen
Key Laboratory for Ultrafine Materials of Ministry of Education
School of Materials Science and Engineering
East China University of Science and Technology
Shanghai 200237, China
E-mail: chenly@ecust.edu.cn

T. Xu, X. Yu
Department of Materials Science
Fudan University
Shanghai 200433, China
E-mail: yuxuebin@fudan.edu.cn

L. Xu, L. Zhang
Jiangsu Key Laboratory for Chemistry of Low-Dimensional Materials
School of Chemistry & Chemical Engineering
Huaiyin Normal University
Huaian 223300, China
E-mail: xl@hytc.edu.cn

L. Wang
Institute for Sustainable Energy/College of Science
Shanghai University
Shanghai 200444, China
E-mail: wlinlin@mail.ustc.edu.cn

The ORCID identification number(s) for the author(s) of this article can be found under https://doi.org/10.1002/smll.202512490

DOI: 10.1002/smll.202512490

spacing (≈0.98 nm), which is conducive to fast electron transport and ion diffusion, inducing fast charging and discharging.[7] However, the thermodynamic instability of pure 1T-MoS_2 requires stabilization by chemical intercalation, introduction of alkali metals, and construction of heterojunctions.[8] Unfortunately, these methods still cannot solve its structural fragility at high current density.[9] Therefore, single-phase MoS_2 often fails to resolve the inherent trade-off problem: fully transformed 1T-MoS_2 lacks long-term structural stability at high current density, while pure 2H-MoS_2 exhibits sluggish kinetic characteristics.

In order to fully utilize the advantages of the two phases of MoS_2, researchers have attempted to manipulate the phase structure of the metallic 1T phase and the semiconductor 2H phase MoS_2 through phase engineering strategies to optimize its electrochemical performance.[10–13] For example, by annealing 2H-MoS_2 with phosphorus vapor at a high temperature of 1000 degrees, phosphorus atoms can occupy the gaps between MoS_2 layers or embed into the lattice, thereby inducing partial transformation of the 2H phase to the 1T phase.[14] This 1T-2H phase MoS_2 not only significantly improves the electrical conductivity, but also exhibits ultra-long electrocatalytic stability. In addition, the lithium ions are utilized to insert into the MoS_2 interlayer through chemical lithiation to achieve the transformation from the 2H phase to the 1T phase, thereby expanding the interlayer spacing and improving the ion transfer efficiency.[15] However, existing phase engineering strategies face a key limitation: conventional intercalation methods (e.g., chemical lithiation or steam annealing) are difficult to control the ratio of 1T and 2H phases, and cannot effectively balance the trade-off between the structural stability of 2H-MoS_2 and kinetic properties of 1T-MoS_2, thereby limiting the long-term stability of electrode materials at high current density and further improvement of electrochemical performance. Therefore, precise control of the ratio of 1T to 2H phase remains a major challenge, which is crucial for optimizing the properties of active materials.[16] Additionally, the existing modification often ignores the synergistic effect between phase engineering and protective carbon hybridization. The protective carbon hybridization can further enhance its stability and conductivity through the integration with active material.[17] However, conventional polymer-derived carbon composites often face two opposing challenges. Polymers with high steric hindrance (e.g., polyaniline) cannot intercalate into MoS_2 interlayers, yielding exclusively 2H-MoS_2 with contracted interlayer spacing.[18] Conversely, low-steric-hindrance polymers (e.g., polyethylenimine) fully penetrate the interlayer spaces, producing purely 1T-MoS_2 with expanded interlayer distance.[19] Both scenarios lead to single-phase MoS_2, fundamentally limiting the simultaneous achievement of carbon compositing and heterostructure engineering. Inspired by the intention, a specific organic molecule is proposed to selectively adsorb the end group of MoS_2 by its large steric effect to achieve partial intercalation of MoS_2 by linear polymer molecules of small steric effect, which is defined as differential intercalation. Based on this, the hybrid phase and carbon combination can be synchronized after heat treatment.

Herein, the realization of differential intercalation is to use the adsorption of phytic acid molecules to block partial 1T-MoS_2, thereby preventing pyrrole monomers from entering the interlayers of these MoS_2. Upon initiator addition, the interlayer 1T-MoS_2 fragments containing pyrrole are connected in series under the action of polypyrrole linear polymerization. At the same time, the polypyrrole chains between the MoS_2 fragments form hydrogen bonds with the capped phytic acid molecules, so that the intercalated and non-intercalated MoS_2 nanosheets are interwined. After annealing, the unintercalated 1T- MoS_2 is converted into 2H MoS_2, which generates heterostructures with the intercalated 1T-MoS_2. These heterogeneous MoS_2 nanosheets (T/H–MoS_2) are sandwiched between the inner nitrogen-doped carbon (NC) nanotubes and the outer N/P co-doped carbon (NPC) layers, forming the NC@T/H–MoS_2@NPC architecture. The electrochemical investigation and DFT calculations reveal that the heterostructures of T/H–MoS_2, as well as the structure of NC intercalation, have a significant promotion effect on ion migration, conductivity, and adsorption, which endows electrode material with the ability of ultralong and ultrafast lithium/sodium storage.

2. Results and Discussion

The schematic for synthesis and structure of NC@T/H–MoS_2@NPC is illustrated in **Figure 1**. The process initiates with the MoO_3 nanorods as the precursor synthesized from molybdenum powder. Subsequently, a polypyrrole (PPY) layer is in situ polymerized on the MoO_3 surface, resulting in the formation of core-shell MoO_3@PPY nanocomposites. As shown in Figure 1a, an anion-exchange reaction is carried out on the polypyrrole tube using thiourea as the sulfur source to produce 1T-phase MoS_2 (T-MoS_2) with large layer spacing (0.98 nm) anchored on the polypyrrole tube (PPY@T–MoS_2). At the same time, the internal MoO_3 nanorods are consumed, thus converting into a hollow structure. Next, the T-MoS_2 is treated with polypyrrole coating and intercalation (Figure 1b). Polypyrrole, being a linear conductive polymer with very small cross-section, facilitates complete intercalation into the MoS_2 interlayers. Notably, phytic acid (PA) plays a crucial role in modulating the intercalation behavior of polypyrrole into MoS_2 during this process, thereby inducing a heterogeneous intercalation structure. After annealing, T-MoS_2 with polypyrrole inserted between the layers retains the original 1T phase with large spacing (0.98 nm), while the non-intercalated portion transforms into the more thermodynamically stable 2H-phase MoS_2 (H-MoS_2) with a smaller interlayer spacing (0.62 nm).

It should be additionally noted that since pyrrole monomer and phytic acid are introduced into the system together, the polymerization reaction is initiated only after thorough mixing. Since the Mo—S bond is a polar covalent bond, the shared electrons will be more on the side of the more electronegative S atom. The results of Bader charge analysis are listed in Table S1 (Supporting Information). The initial charge of Mo atoms decreases from 14 to 13, while the S atoms increase from 6 to ≈6.5. As a result, the charge will be closer to the S-atom layer on both sides, which leads to localized positively charged regions at the middle Mo-atom layer (Figure S1, Supporting Information). In addition, peroxidized Mo^{6+} may appear at the edges of the layer, which can also contribute to the formation of localized positive charges.[20] Therefore, MoS_2 will preferentially attract the more nucleophilic phytic acid molecules (Figure 1c). The large site resistance of the phytic acid molecules prevents them from entering the interlayer

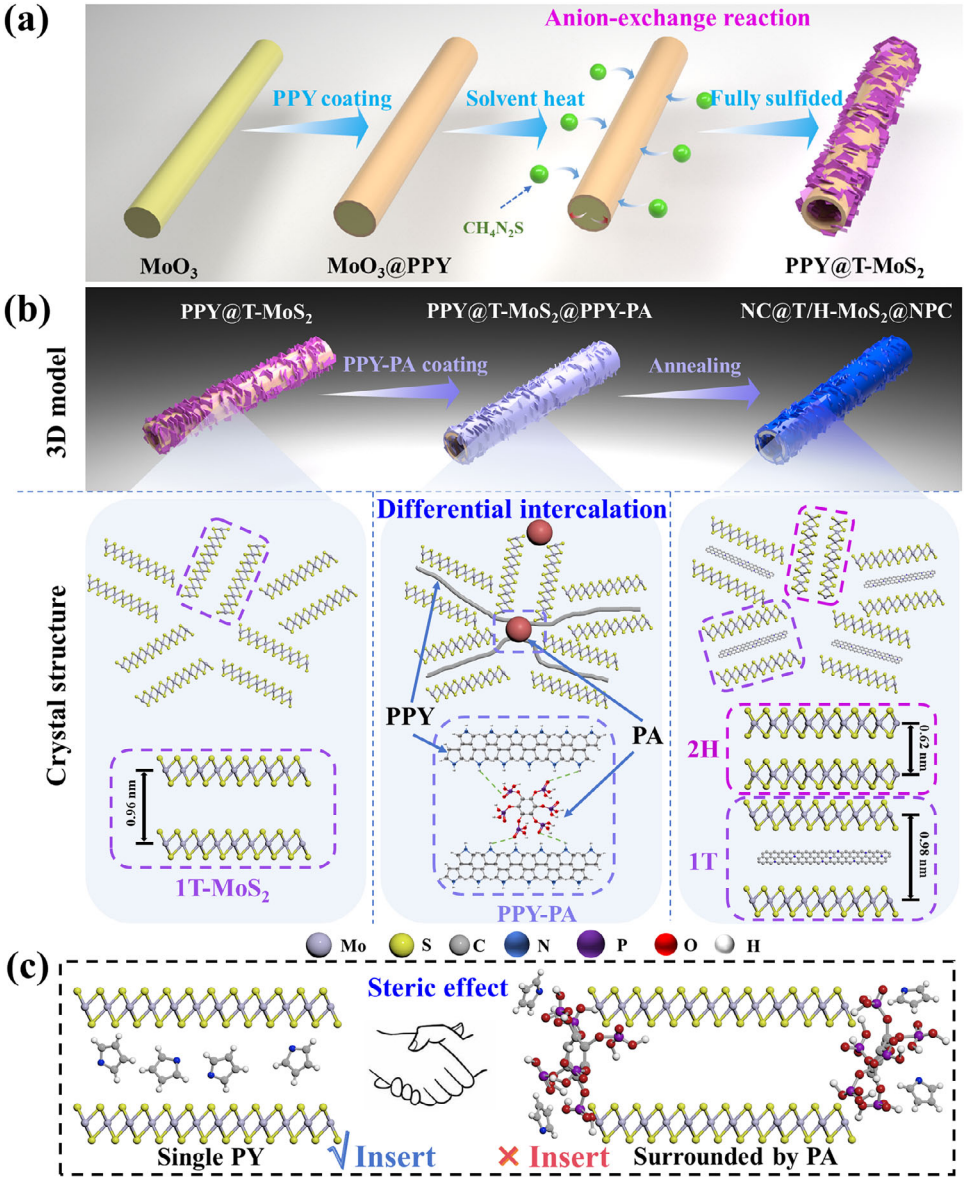

Figure 1. a) Flowchart of the preparation of PPY@T–MoS_2 precursor. b) Schematic 3D models and crystal structures of NC@T/H–MoS_2@NPC. c) Schematic diagram of differential intercalation of MoS_2 by phytic acid and pyrrole monomers.

of 1T-MoS_2, and they can only exist in the periphery by electrostatic adsorption, forming a "barrier". Therefore, it is difficult for pyrrole monomer to enter the interlayer of 1T-MoS_2 in the area where phytic acid is present.

This constitutes a prerequisite for the formation of differential intercalation. Ultimately, the MoS_2 without pyrrole monomer between the layers cannot yield an intercalation of polypyrrole at the end of the polymerization reaction, while the rest can. The carbon layer converted from polypyrrole is nitrogen-doped carbon noted as NC, which is nitrogen- and phosphorus-co-doped carbon from phytate-cross-linked polypyrrole is noted as NPC. As a result, the final sample (NC@T/H–MoS_2@NPC) drives the 1T and 2H phase heterostructures. As plotted in Figure S2 (Supporting Information), PPY@T–MoS_2 is directly annealed to obtain NC@H–MoS_2, where MoS_2 is confirmed to be 2H phase. Annealing after coating of PPY without the addition of phytate yielded NC@T–MoS_2@NC, where MoS_2 is confirmed to be 1T phase. These confirmations for the phase of MoS_2 will be described in the subsequent characterization.

2.1. Morphological and Physical Characteristics

As a precursor, MoO_3 has good crystalline and without other impurities (Figure S3, Supporting Information).[21] The XRD patterns of NC@T/H–MoS_2@NPC with different phytic acid additions are explored in **Figure 2a**. Suffixed numbers denote the addition volume of 0.1, 0.2, 0.5, 1, and 2 mL of phytic acid solution added, respectively. The peak located at 9° represents the large-spaced 1T phase labeled as $(002)^{1T}$, while the peak located at 13.6°

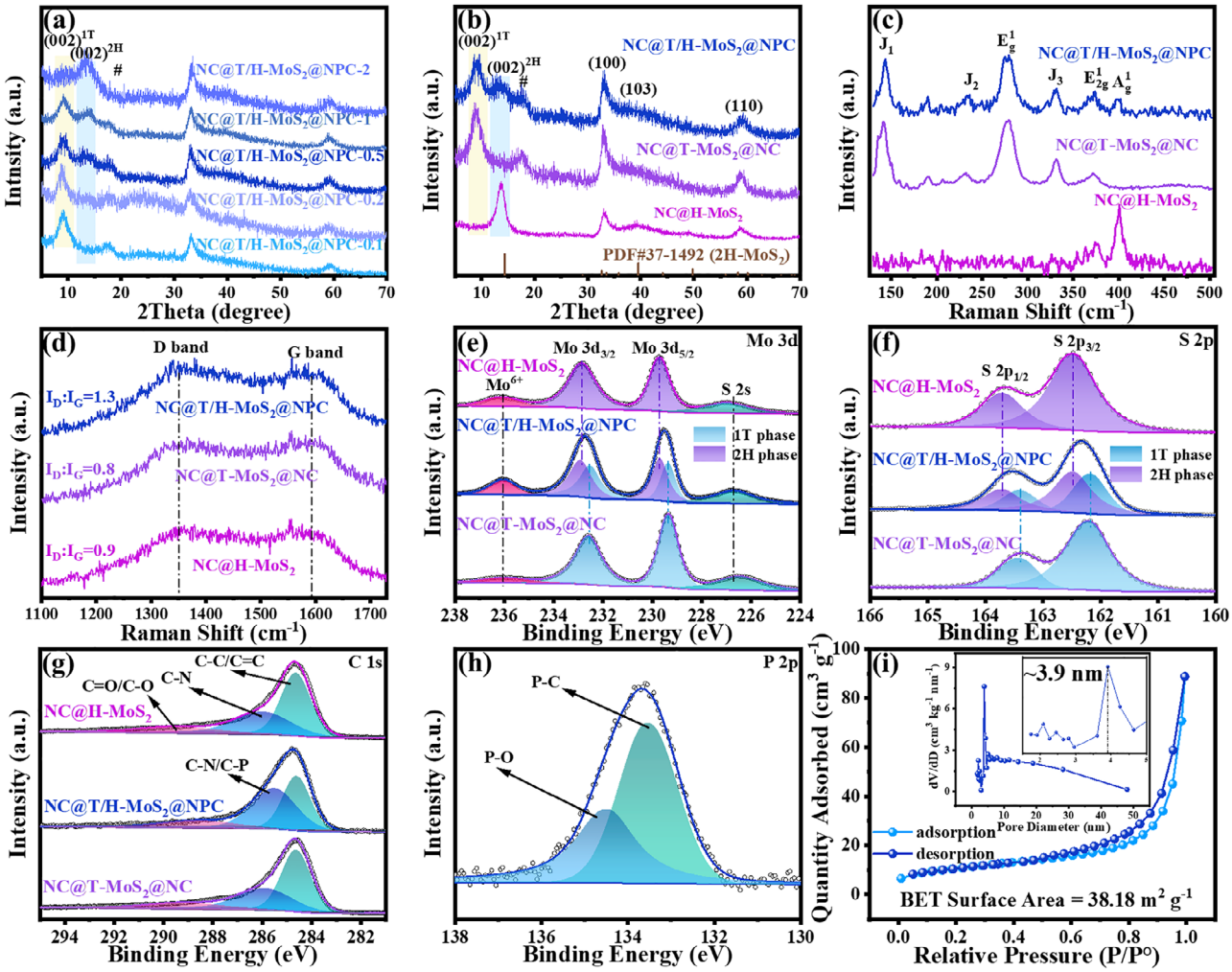

Figure 2. a) XRD patterns of NC@T/H–MoS_2@NPC with different phytic acid additions. (The sample with phytic acid addition of 0.5 mL is chosen as the representative for the subsequent tests.) b) XRD patterns of different phases of MoS_2. c,d) Raman spectra of MoS_2-based composites; High-resolution XPS spectra for e) Mo 3d, f) S 2p, g) C 1s, and h) P 2p; i) Nitrogen adsorption and desorption curves and pore size distribution result as an inset for NC@T/H–MoS_2@NPC.

represents the small-spaced 2H phase labeled as $(002)^{2H}$.[4] As the amount of phytic acid increases, the strength of $(002)^{1T}$ gradually weakens, while the intensity of $(002)^{2H}$ gradually strengthens. Specifically, plot the ratio of peak intensities of them (I_{1T}/I_{2H}) against the amount of phytic acid added, as shown in Figure S4a (Supporting Information). After taking the logarithm of I_{1T}/I_{2H}, the graph (Figure S4b, Supporting Information) shows a linear relationship. The specific values covered in the figure are listed in Table S2 (Supporting Information). Controlled adjustment of the mixing phase ratio is basically realized. This confirms that the phytic acid addition is inversely proportional to the intercalation behavior. After annealing, the large-spaced 1T phase gradually decreases. To simplify the following analysis, NC@T/H–MoS_2@NPC with 0.5 mL addition is chosen as a representative for the subsequent characterization and electrochemical test.

In Figure 2b, the unintercalated NC@H–MoS_2 matches the standard card for 2H-phase MoS_2 (PDF #37-1492), and the peak located near 13.6° corresponds to the $(002)^{2H}$ interplane spacing, which is calculated to be 0.62 nm according to Bragg equation. The fully intercalated NC@T–MoS_2@NC by polypyrrole displays an extended layer with the crystallographic surface shifted to 9° labeled $(002)^{1T}$ to differentiate it from the pre-expanded crystallographic surface, which means that the layer spacing is extended to 0.98 nm. It is noteworthy that a new peak appears near 17.8° (noted as # in the figure), with a calculated layer spacing of 0.49 nm exactly half of 0.98 nm. This represents the distance from the carbon layer inserted between the layers to the MoS_2 layers on either side. After the intercalation behavior occurs, the (103) crystalline surface becomes inconspicuous, representing a different arrangement of the coordination modes of Mo and S along the in-plane direction, which implies that the phase transformation from trigonal 2H MoS_2 to octahedral 1T MoS_2. The NC@T/H–MoS_2@NPC, as partially intercalated sample, exhibits the appearance of peaks at all three positions mentioned above, which indicates the presence of both 0.62 and 0.98 nm layer-spaced MoS_2 in the composite. This result suggests that 1T phase and 2H phase MoS_2 are in a coexistence state.

The phase discrimination between 1T- and 2H–MoS_2 is clearly provided in Figure 2c by Raman spectra. For NC@H–MoS_2, the peaks at 373 and 400 cm^{-1} are attributed to the out-of-plane Mo–S (E^1_{2g}) and in-plane Mo–S (A^1_g), both of which are characteristic peaks belonging to the 2H phase MoS_2.[22] For NC@T-MoS_2@NC, there are five peaks at 141, 234, 278, 331, and 373 cm^{-1} corresponding to the J_1, J_2, E^1_g, J_3 and A^1_g modes of 1T phase MoS_2.[23] After modulation with phytate, the NC@T/H-MoS_2@NPC composite exhibits all six characteristic vibrational modes, with clearly resolvable peaks from both phases, providing unambiguous evidence for the heterogeneous coexistence of 1T and 2H phases within the material. Comparing with the intensity of D and G bands (Figure 2d), the I_D/I_G of NC@T/H-MoS_2@NPC is 1.3, which is higher than the other two samples, because the additional doping of P creates more defects in the carbon layer.[24] Actually, the appearance of phosphorus can be traced back to the involvement of PA. The extra outgoing peak at 1281 cm^{-1} for PPY@T-MoS_2@PPY-PA before annealing represents the presence of P═O in FTIR result (Figure S5, Supporting Information).[25] Moreover, the displacement of hydrogen bonding can be observed in the magnified image of the fingerprint region, and these confirm that the phytic acid is indeed cross-linked into the polymer network. These PA-derived defects can provide additional adsorption sites for Li^+/Na^+ and accelerate ion transport.[26]

To further verify the 1T and 2H phases of MoS_2, XPS analysis is performed to disclose the bonding forms. Five elements, O, N, C, Mo, S, and P are detected in the full spectrum of NC@T/H–MoS_2@NPC (Figure S6, Supporting Information), which corresponds to the elements included in the chemical formula. In the 1T and 2H phases, there is no difference in the coordination environments of Mo^{6+} with S. Therefore, the peaks attributed to Mo^{6+} in Figure 2e appear at the same location for three samples, which are all located at 236.1 eV without shifts.[14] However, for the Mo $3d_{3/2}$, Mo $3d_{5/2}$, and S 2s spectra, they are influenced by the coordination environments of the 1T and 2H phases and get shifted.[27] Typically, the peaks at 229.5 and 232.7 eV correspond to the 2H phase MoS_2, while 229.2 and 232.5 eV correspond to the 1T phase.[28,29] Similarly, the shift between S $2p_{1/2}$ and S $2p_{3/2}$ in the S 2p spectrograms (Figure 2f) also hints at the difference in phase composition.[30] The peaks located at 162.2 and 163.4 eV are the 1T phase, while the peaks at 162.5 and 163.7 eV correspond to the 2H phase.[15,31] Based on the contents of the above two spectra, it is verified that MoS_2 in NC@H–MoS_2, NC@T–MoS_2@NC, and NC@T/H–MoS_2@NPC are 2H phase, 1T phase, and 1T-2H hybrid phase, respectively. It should be added that the characteristic peak (184.6 eV) corresponding to —C—S—C— is observed in the wider range of S 2p spectrum (Figure S7, Supporting Information).[32] This implies that part of the sulfur is doped into the carbon network, further increasing the defect structure. And this may also cause sulfur vacancies on MoS_2, providing additional paths for alkali metal ions to migrate between MoS_2 layers. In the C1s spectrum (Figure 2g), due to the co-doping of N and P, the fitted peak position of C—N/C—P in NC@T/H–MoS_2@NPC shows a significant rightward shift compared to the two samples doped with N alone. This is due to the weaker electronegativity of P compared to N, resulting in lower binding energy with C. The common types of nitrogen are detected as pyrrole nitrogen, pyridine nitrogen, and quaternary nitrogen (Figure S8, Supporting Information), combined with the analysis of P and C spectra, which confirms that the carbon in the material is in the N/P rich co-doped state. The peaks located at 133.1 and 134.2 eV in the P 2p spectra (Figure 2h) are attributed to P—C and P—O, which can be further verifies that PA has successfully cross-linked PPY.[24] Furthermore, it is noteworthy in the N spectrum that Mo—N is detected at 395.5 eV.[33] This indicates the formation of chemical bonds between the N-doped carbon network and MoS_2. At the same time, N replaces some of the positions of S, resulting in sulfur vacancies.

Electron paramagnetic resonance (EPR) spectroscopy provides direct evidence for the existence of sulfur vacancies in the MoS_2 structure (Figure S9, Supporting Information). The characteristic signal at g = 2.004 is attributed to unpaired electrons associated with sulfur vacancies and oxygen vacancies, with the intensity variation clearly demonstrating that the sandwich-structured samples (NC@T/H–MoS_2@NPC and NC@T–MoS_2@NC) possess significantly more vacancies than the single-layer counterpart (NC@H–MoS_2).[22] These vacancies will be more conducive to ion transport, while the sandwich structure constructed through chemical bonds will provide a robust skeleton. The adsorption and desorption curves of NC@T/H–MoS_2@NPC are tested using nitrogen as the carrier gas, and the results are shown in Figure 2i, with the S_{BET} of ≈38.18 $m^2\ g^{-1}$. The sample exhibits a bimodal pore size distribution, with micropores (2 nm) and mesopores (10 nm) jointly contributing to the high specific surface area. It is well known that mesopores can promote ion migration, while micropores can act as active sites for the adsorption of Li^+/Na^+.[34] The BET results of the two contrast samples are summarized in Figure S10 (Supporting Information). For NC@T–MoS_2@NC (Figure S10a, Supporting Information), the S_{BET} is 32.07 $m^2\ g^{-1}$ while that for NC@H–MoS_2 (Figure S10b, Supporting Information) is 28.60 $m^2\ g^{-1}$. The fact that NC@T/H–MoS_2@NPC contains the highest specific surface area can be attributed to the additional hydrogen- and oxygen-containing energetic groups brought by the phytic acid molecules, which can generate more hydrogen and oxygen during the annealing process, resulting in more pore structures when spilling out of the bulk phase of the material. The content of carbon and MoS_2 in the composites is analyzed with thermogravimetric (TG) curves (Figure S11, Supporting Information). Pure MoS_2 is chosen as a comparison, and the weight decays to 87.2% when heated to 700 °C under air atmosphere. Under the same conditions the mass of NC@T/H–MoS_2@NPC decays to 73.1%. It can be determined that the carbon content in the NC@T/H–MoS_2@NPC composite is 14.1 wt.%.

The morphology of the various stages of the preparation process is recorded with scanning electron microscope (SEM). MoO_3 as precursor in **Figure** 3a exhibits a uniform rod-like structure accompanied by a smooth surface. This lays the foundation for the subsequent construction of nanotubular structures. After in situ coating of polypyrrole, the surface becomes rough and the nanorods are slightly coarsened (Figure 3b). Upon vulcanization, the surface of the nanotubes grows distinct flaky of MoS_2 (Figure 3c). When the outer layer is coated with another layer of

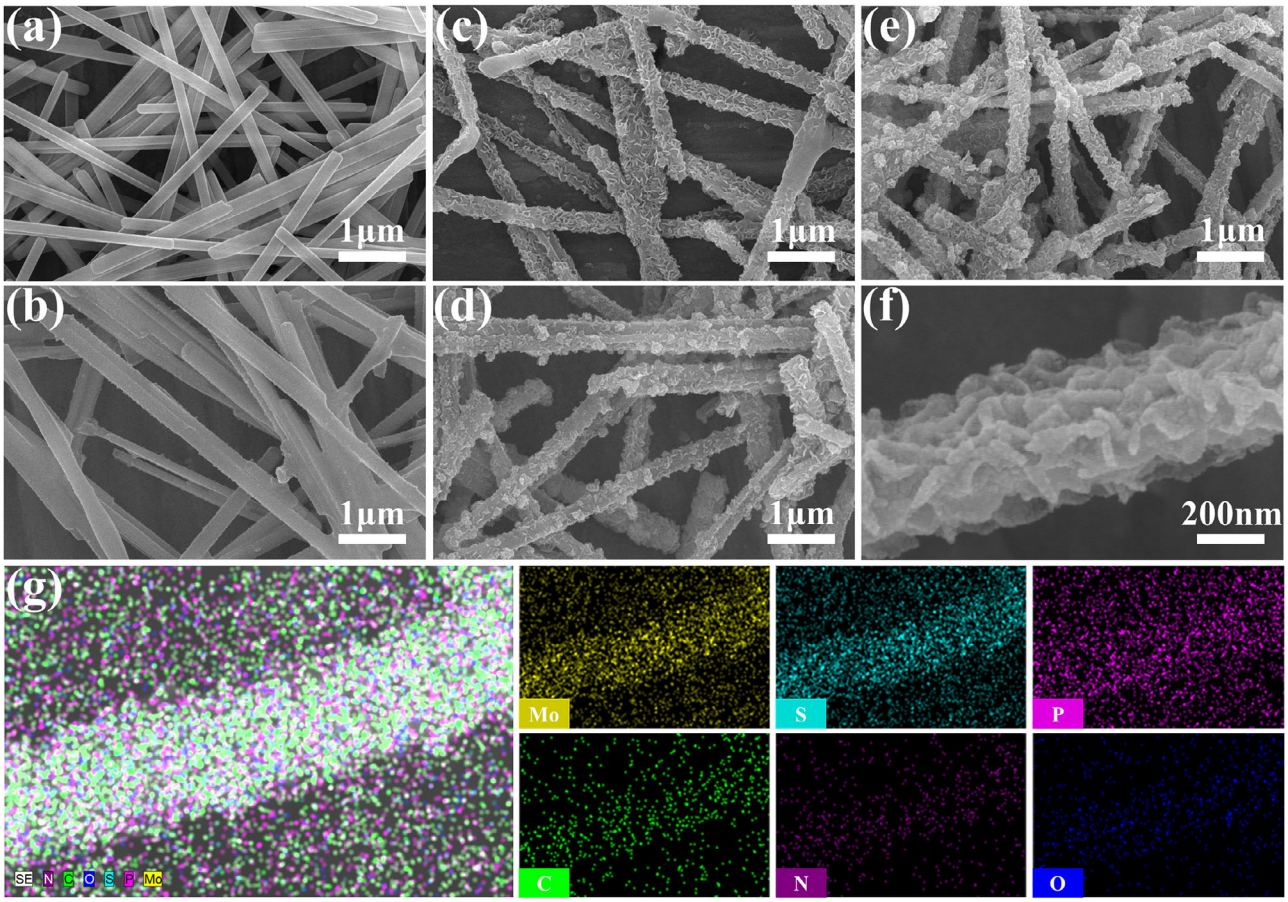

Figure 3. FESEM images of corresponding samples: a) MoO_3, b) MoO_3@PPY, c) PPY@T–MoS_2, d) PPY@T–MoS_2@PPY-PA, e,f) NC@T/H–MoS_2@NPC; g) Elemental mappings for NC@T/H–MoS_2@NPC.

phytic acid cross-linked polypyrrole to form a sandwich structure of PPY@T–MoS_2@PPY-PA (Figure 3d), the flaky MoS_2 on the surface is not as obvious as before. In order to enhance the conductivity, the polymer is transformed into N/P-doped carbon by annealing under nitrogen atmosphere. As shown in Figure 3e, the high temperature does not destroy the structure of carbon tubes and flaky MoS_2. After scanning one of the nanotubes with energy dispersive spectrometer (EDS), a uniform distribution of N, C, O, S, P, and Mo can be detected in the spectrograms of the elemental mappings (Figure 3f,g). The SEM images of NC@H–MoS_2 and NC@T–MoS_2@NC as two comparison samples are shown in Figure S12 (Supporting Information). The whole morphology remains tubular, with the nanosheets more obvious in NC@H–MoS_2 where the outer layer is not blocked.

In order to further explore the structure of NC@T/H–MoS_2@NPC and the 1T-2H heterostructure for different layer spacings, high-resolution transmission electron microscopy (HRTEM) is performed. **Figure** 4a confirms the hollow tubular structure with flakes of MoS_2 loaded on the surface. Two different layer spacings of MoS_2 are observed in Figure 4b. Measurement in sites A and B shows consistent results with XRD, exhibiting the 0.62 and 0.98 nm layer spacings. The other two areas are selected to observe the diffraction rings in the part with uniform layer spacing. The results show that the diffraction rings exhibit a 1T pattern (Figure 4d) in the region with the layer spacing of 0.98 nm and a 2H pattern (Figure 4e) in the region with 0.62 nm.[35,36] The presence of the two phases also converges with the results of the Raman and XPS analyses. This confirms the existence for the 1T-2H heterostructure MoS_2 in NC@T/H–MoS_2@NPC. And there is a correspondence between the large/small layer spacing and the 1T/2H phase. The lattice stripes are further differentiated in Figure 4c, with the thick stripes representing the MoS_2 layer and the thin ones the carbon layer.[37] It is interesting to note that the carbon layer is always present between the layers of MoS_2 with 0.98 nm layer spacing, while the 0.62 nm one is absent. And the carbon layer is located at the centered position of the two MoS_2 layers, with the distance of 0.49 nm (0.98/2 nm) to the sides, which corresponds to the peak appearing near 17.8° (noted as #) in Figure 2b. Combined with the analysis of the diffraction rings, it appears that the insertion of the carbon layer results in both large layer spacing and 1T phase. When observing high-resolution lattice fringes in another region (Figure 4f), it is noticed that these 2D layered MoS_2 have a large number of defects, which will facilitate ion shuttle.

In the previous analysis, carbon insertion, large layer spacing, and the 1T phase always co-exist. Furthermore, in Figure 2a, it is noteworthy that the large-spaced 1T-MoS_2 gradually decreases and eventually nearly disappears as the amount of phytic acid

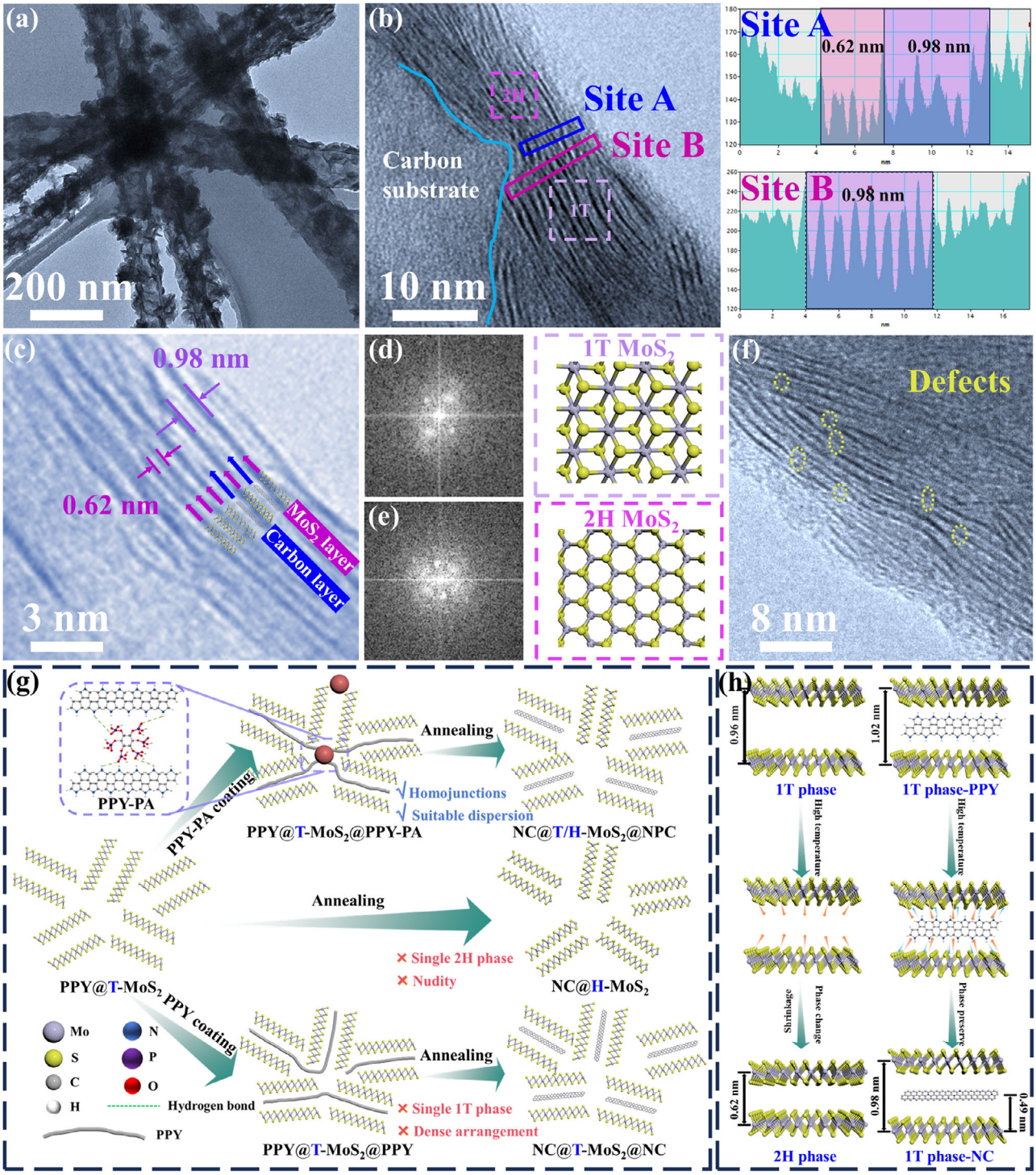

Figure 4. a) TEM and b,c,f) HRTEM images of NC@T/H–MoS_2@NPC; d,e) Diffraction rings at two corresponding positions in Figure 4b and schematic diagrams of the structure of 1T and 2H phase MoS_2; Schematic representation for g) The formation history of MoS_2 in three different phases and h) The effect of whether PPY is inserted between layers on the phase transition during annealing process.

increases. Therefore, it becomes necessary to explore the intrinsic connection among them. The formation history of three different phases of MoS_2 is plotted in Figure 4g. PPY@T–MoS_2 as a precursor is identified by XRD (Figure S13, Supporting Information) and Raman (Figure S14, Supporting Information), where the MoS_2 is the 1T phase with 0.96 nm layer spacing. Thus, it is not the interpolation that has caused the expansion of the layer spacing and the phase transition, but the MoS_2 formed after the high-temperature hydrothermal process is already 1T phase with large layer spacing. However, if annealing is taken directly, this structure cannot be retained and collapses into the thermodynamically more stable 2H phase with small layer spacing, as demonstrated by the XRD, Raman, and XPS results of NC@H–MoS_2. The MoS_2 thus obtained is not only a pure 2H phase but also directly exposed. Afterward, the intercalation and coating of PPY@T–MoS_2 with either polypyrrole alone or phytate-cross-linked polypyrrole (PPY@T–MoS_2@PPY and PPY@T–MoS_2@PPY–PA) is carried out at room temperature, which cannot affect the crystal structure of MoS_2 in the precursor (PPY@T–MoS_2), except for a small increase in the layer spacing (0.96 to 1.02 nm). Therefore, PPY@T–MoS_2@PPY and PPY@T–MoS_2@PPY–PA in Figure S13 (Supporting Information) also exhibit the diffraction pattern of the 1T phase with large layer spacing. Here, the intercalation space of the 1T phase and the volumes of phytate and polypyrrole need to be screened. The calculated spacing (9.6 Å) using the (002) crystal plane in XRD is the spacing of two Mo atomic layers, but the actual intercalation process needs to take into account the spacing of two S atomic layers (Figure S15a, Supporting Information), which is calculated to be 6.0 Å. After simulating the volume of phytic acid molecules (Figure S15b, Supporting Information), the volume parameters along the three directions of the a, b, and c axes are 6.80, 13.52, and 12.32 Å, all of which are larger than the spacing between the two sulfur atom layers. Therefore, phytic acid is considered to be unable to insert into the interlayer of MoS_2. The volume parameters of the pyrrole monomer along the three directions are 3.20, 6.26, and 6.52 Å, respectively (Figure S15c, Supporting Information). The size in the *a*-axis direction is much smaller than 6.0 Å, so the pyrrole monomer can enter into the interlayer of MoS_2. What's more, the pyrrole monomer is a bifunctional group and can only be linearly polymerized along the *c*-axis direction (Figure S15d, Supporting Information). The conjugated structure on the polypyrrole chain segments ensures that all atoms are in the same plane, and thus the process of polymerization does not significantly increase the size in the *a*-axis direction (Figure S15e, Supporting Information). Thus, the small site resistance effect of the linear polypyrrole could allow them to achieve full intercalation of MoS_2 with 0.96 nm layer spacing, as plotted for PPY@T–MoS_2@PPY in Figure 4g. During the annealing process, the tandem interaction of linear polypyrrole on MoS_2 leads to dense arrangement, thus leaving insufficient space for releasing the volume expanded by the Li^+/Na^+ storage process.

The addition of phytic acid utilizes hydrogen bonding to achieve cross-linking of the polypyrrole, which transforms the linear polymer into network structure. As previously described, prior to polymerization phytic acid is preferentially adsorbed on a portion of MoS_2 resulting in blocking. This will prevent the pyrrole monomer from entering the interlayers of this portion of MoS_2, which in turn achieves the effect of differential intercalation of polypyrrole on MoS_2 after polymerization. The homogeneous structure with large-spaced 1T phase and small-spaced 2H phase is thus formed after annealing, as plotted on the structural schematic of NC@T/H–MoS_2@NPC in Figure 4g. In Figure 2a, as the phytic acid addition increases, the blocking action is more and more frequent, making the pyrrole monomer less accessible to the interlayers, and thus less MoS_2 is retained in the large interlayer spacing after annealing. When the phytic acid addition is increased to 2 mL, the intercalation phenomenon almost fails to occur, and all of them are transformed into small-spaced 2H–MoS_2 after annealing. Compared to fully intercalated NC@T–MoS_2@NC, in the differential intercalation system (NC@T/H–MoS_2@NPC), MoS_2 can be more uniformly dispersed into the carbon matrix. The evolution of MoS_2 with or without polypyrrole protection between layers during annealing is visually plotted in Figure 4h. Since the simple 1T phase MoS_2 is thermodynamically unstable, the originally large interlayer spacing shrinks at high temperatures with a concomitant phase transition to the thermodynamically more stable 2H phase. When the interlayers are protected by polypyrrole, this shrinkage can be resisted thus maintaining MoS_2 as a 1T phase with large layer spacing. Linear polypyrrole turns into nitrogen-doped carbon layers and retains in the interlayers of the 1T phase.

2.2. Electrochemical Properties of LIBs

The actives are assembled into lithium-ion half-cells to test their performance in storing lithium ions. At a small current density of 0.5 A g^{-1} (**Figure 5a**), there is little difference in performance among the three samples. The galvanostatic charge/discharge (GCD) curves of NC@T/H–MoS_2@NPC are shown in Figure S18a (Supporting Information), and after the first lap, the curves have a good overlap, suggesting reversible cyclic stability. In the test of rate performance (Figure 5b), after going through different current densities from 0.1 to 10 A g^{-1}, the capacity of NC@H–MoS_2 has shown a significant decay. The other two samples with sandwich structures show smooth capacity. This confirms the necessity of the sandwich structure to prevent direct contact of MoS_2 with the electrolyte.

Interestingly, in the comparison of NC@T–MoS_2@NC and NC@T/H–MoS_2@NPC, the capacity of NC@T/H–MoS_2@NPC is higher at small current densities, and the difference in capacity between them decreases as the current density increases. When the current density is increased to 8 and 10 A g^{-1}, NC@T–MoS_2@NC shows higher capacity. This is because MoS_2 in NC@T–MoS_2@NC is the pure 1T phase with large layer spacing, whereas in NC@T/H–MoS_2@NPC it is the hybrid phase. In the case of MoS_2, the capacity of the pure large-spaced 1T phase is certainly higher than that of the hybrid phase. However, due to the additional P doping in the carbon layer of NC@T/H–MoS_2@NPC, the active sites exposed by these dopants make up for the capacity gap caused by the two types of MoS_2 at small current densities. To differentiate the capacity contributions of carbon and T/H–MoS_2 in NC@T/H–MoS_2@NPC composites, the rate properties of pure polypyrrole-derived nitrogen-doped carbon (NC) are documented in Figure S16a (Supporting Information). The capacity contribution (C_{MoS2}) of T/H–MoS_2 can

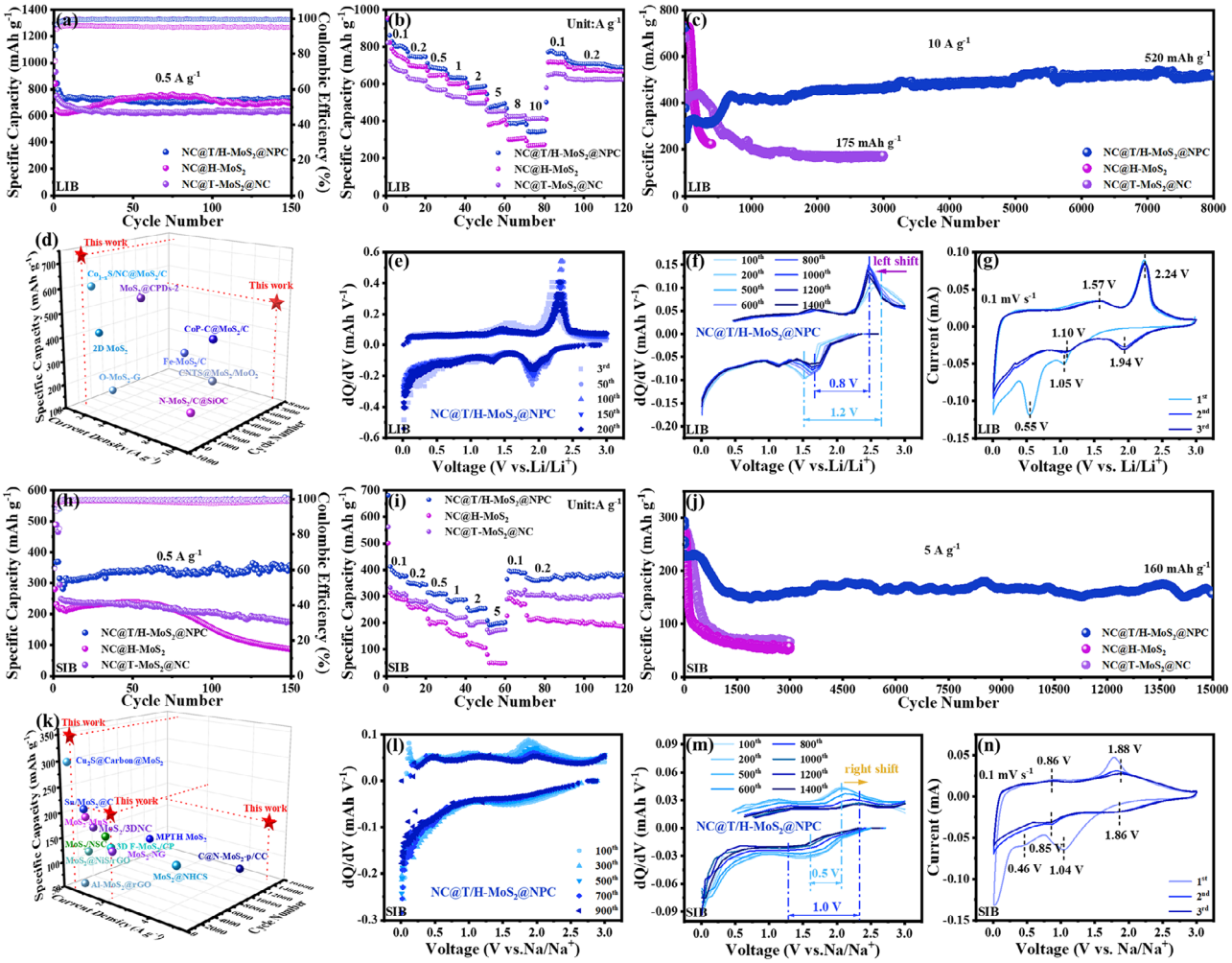

Figure 5. Cycling performance at a) 0.5 A g^{-1} and c) 10 A g^{-1} for LIB. b) Rate performance for LIB. d) Performance comparison with other MoS_2 materials used as anode for LIB. Capacity differential curve at e) 0.5 A g^{-1} and f) 10 A g^{-1} current density for NC@T/H–MoS_2@NPC in LIB. g) CV curves of NC@T/H–MoS_2@NPC at 0.1 mV s^{-1} in LIB. Cycling performance at h) 0.5 A g^{-1} and j) 5 A g^{-1} for SIBs. i) Rate performance for SIB. k) Performance comparison with other MoS_2 materials used as anode for SIB. Capacity differential curve at l) 0.5 A g^{-1} and m) 5 A g^{-1} current density for NC@T/H–MoS_2@NPC in SIB. n) CV curves of NC@T/H–MoS_2@NPC at 0.1 mV s^{-1} in SIB.

be calculated using Equations S1–S3 (Supporting Information). Take the calculation at 0.1 A g^{-1} current density as an example. At this time, $Q_{composite}$ can be read as 806 mAh g^{-1} (fifth circle data at various current densities) in Figure 5b, and Q_C can be read as 707 mAh g^{-1} in Figure S16a (Supporting Information). According to the analytical results of thermogravimetry, f_{MoS2} is 0.859, and f_C is 0.141. It can be calculated that C_{MoS2} is 87.7%. The calculated capacity contribution of MoS_2 at other current densities is summarized in Figure S16b (Supporting Information). The capacity contribution of MoS_2 gradually increases with increasing current density. It can be seen that this contribution increases slowly when the current density is small (0.1–2 A g^{-1}). As the current density increases to 5–10 A g^{-1}, a rapid increase is evident. These two growth stages are basically consistent with the capacity comparison results between the hybrid phase MoS_2 (NC@T/H–MoS_2@NPC) and pure 1T phase MoS_2 (NC@T–MoS_2@NC) in Figure 5b. In addition, lattice distortion caused by heterostructures may also lead to more defects and cavity structures, which will provide additional adsorption and filling sites for Li^+. As the current density increases, these defects and cavity structures gradually become unable to compensate for the capacity gap caused by the phase structure. Consequently, the capacity of NC@T/H–MoS_2@NPC dominates at small current densities, while NC@T–MoS_2@NC is higher at high current densities.

However, the rate performance is difficult to distinguish the cycling stability of the electrode materials, so the long-term cycling performance of these three electrodes at the current density of 10 A g^{-1} is further compared in Figure 5c. Under the impact of the huge current density, the performance of the three electrodes appeared to be significantly different. The importance of structural stability brought about by hybrid phases is magnified. It can be seen that the 1T-phase MoS_2 with large layer spacing (NC@T–MoS_2@NC) reveals a significant capacity decay after 300 cycles, whereas the 1T-2H phase MoS_2 (NC@T/H–MoS_2@NPC) exhibits amazing

stability, maintaining a stable capacity of 520 mAh g^{-1} after 8000 cycles. This ability to charge and discharge rapidly over long terms stands out in comparison with other MoS_2 system materials, as plotted in Figure 5d. The specific dates involved in the figure are listed in Table S3 (Supporting Information). It also exhibits high capacity at small current density. It is the synergistic effect of the sandwich structure and hybrid–phase engineering that endows NC@T/H–MoS_2@NPC with such outstanding structural stability.

For the NC@T/H–MoS_2@NPC, a significant activation phenomenon occurs ≈500 to 800 cycles, and in order to analyze this phenomenon the capacity differential curve is indispensable. First, at 0.5 A g^{-1} (Figure 5e), a good overlap of the curves can be seen in the NC@T/H–MoS_2@NPC as the number of cycles increases, further verifying the high reversibility of the cycles. For the two comparison samples (Figure S17a,b, Supporting Information), both show different degrees of deformation, exhibiting limited cycling reversibility. Importantly, the oxidation peaks of NC@T/H–MoS_2@NPC show a distinctive left shift under 10 A g^{-1} (Figure 5f). In contrast, both comparison samples (Figure S17c,d, Supporting Information) appear to have a general right shift. Among them, the right shift of NC@H–MoS_2 is the most rapid. Generally speaking, as the cycle progresses, the charge accumulation phenomenon in the electrode material becomes more and more serious, and then polarization occurs, which is reflected in the rightward shift of the oxidation peak. When the polarization builds up to a certain level, for example, the potential at which the oxidation peak appears has exceeded 3 V by the 200th cycle (Figure S17d, Supporting Information), which means that the active material is gradually deactivated. This is reflected in the cycle-capacity curve as a rapid capacity decay, as demonstrated in Figure 5c, where both NC@T–MoS_2@NC and NC@H–MoS_2 show different degrees of capacity decay. As previously presented, the conductivity of 1T-MoS_2 is superior to that of 2H-MoS_2. Hence, the NC@T–MoS_2@NC with 1T-MoS_2 has a slower decay rate. In the case of NC@T/H–MoS_2@NPC, on the other hand, it is not affected by the polarization phenomenon due to the presence of 1T-phase and 2H-phase heterostructure, which can conduct charge faster at the interface. On the contrary, Li^+ has a certain activating effect on the small-spaced 2H-phase MoS_2, which results in the rare phenomenon of a left shift of the oxidation peak, and therefore, a capacity enhancement is observed.

The charge transfer resistance of the electrode materials can be analyzed by electrochemical impedance spectroscopy (EIS) (Figure S18b, Supporting Information) and can be quantified by the software after further drawing the equivalent circuit. The results are listed in Table S4 (Supporting Information), where NC@T/H–MoS_2@NPC possesses the smallest R_{ct} (63.2 Ω). The galvanostatic intermittent titration technique (GITT) is utilized to further explore the reaction kinetics (Figure S19a–c, Supporting Information). The value of diffusion coefficient D for Li^+ is calculated with the help of Equation S4 (Supporting Information). After averaging the logarithm of this value, the results for the three samples are −9.18 (NC@T/H–MoS_2@NPC), −11.70 (NC@H–MoS_2), and −9.82 (NC@T–MoS_2@NC), respectively. Among them, NC@T/H–MoS_2@NPC exhibits the largest value, i.e., possesses the fastest lithium-ion diffusion kinetics. This is due to the Fermi energy gap between the 1T and 2H phases, leading to the triggering of an internal electric field at the heterogeneous interface, which in turn promotes charge transfer.[38] This is an important factor that allows 1T-2H phase MoS_2 to withstand higher current densities compared to the pure 1T phase.

The CV curves of NC@T/H–MoS_2@NPC are tested at a sweep rate of 0.1 mV s^{-1} (Figure 5g). The reduction peaks at 1.05 and 0.55 V during the first turn of discharge correspond to the formation of the solid electrolyte interface (SEI) and the insertion of Li^+ into the interlayer of MoS_2.[39] Two pairs of redox peaks of classical MoS_2 lithiation and delithiation at 2.24/1.94 and 1.57/1.10 V, respectively, are exhibited in the subsequent cycles.[40,41] As the sweeping speed increases, the peak current becomes progressively larger (Figure S18c, Supporting Information). The relationship between peak current and sweep rate (Equations 1 and 2) can be used to qualitatively analyze the capacitance and battery behavior.

$$i = av^b \tag{1}$$

$$\log i = b \log v + \log a \tag{2}$$

After fitting the four peak currents, the b values are 1.2, 0.92, 0.93, and 1.0, respectively (Figure S18d, Supporting Information). Compared to 0.5, the b value is closer to 1, implying that the capacitive contribution dominates. It should be noted that there is a situation where the b value exceeds 1, which may be due to the short and fast ion diffusion path brought by the hollow tubular structure and heterojunction, resulting in a faster actual peak current growth rate than the theoretical value at high scanning rates. Further calculations of the pseudocapacitance contribution are performed, and the capacitance contribution reaches 90% at 1 mV s^{-1} (Figure S18e, Supporting Information). As shown in Figure S18f (Supporting Information), with the increase of scanning speeds, the capacitance control reaches 75%, 80%, 84%, 85%, 87%, and 90%, respectively, gradually occupying the dominant position. This suggests that NC@T/H–MoS_2@NPC has a significant pseudocapacitance effect during the storage of Li^+, a reaction that tends to converge on the surface of the material and endows the electrode material with great cyclic reversibility.

2.3. Electrochemical Properties of SIBs

The large radius of Na^+ places more stringent requirements on the structural stability of the electrode material. At the current density of 0.5 A g^{-1} (Figure 5h), NC@T/H–MoS_2@NPC has already demonstrated a stability that stood out from the other two electrode materials. A high discharging specific capacity of 350 mAh g^{-1} is maintained after 150 cycles. For NC@H–MoS_2, without the protection of the sandwich structure, 2H-MoS_2 is in direct contact with the electrolyte, and the capacity decreases rapidly at the beginning of the cycle. For NC@T–MoS_2@NC, on the other hand, it can last longer, and the 1T-MoS_2 structure is destroyed slower. In the case of the NC@T/H–MoS_2@NPC, the GCD curves (Figure S21a, Supporting Information) show a high degree of overlap, except for the activation in the first lap. Unlike LIBs, the presence of heterostructure greatly accelerates the Na^+ transport, and thus NC@T/H–MoS_2@NPC exhibits much better capacity at all current densities in the rate performance

(Figure 5i). The stability enhancement due to the synergistic effect of the hybrid phase and the sandwich structure in NC@T/H–MoS_2@NPC is manifested at the high current density of 5 A g^{-1} (Figure 5j). The capacity decay phenomenon that occurs in the first 1500 cycles may originate from the initial activation of carbon nanotubes and MoS_2.[42] In addition, the unstable SEI membrane of the sodium-ion battery itself also leads to the inherent capacity decay phenomenon. The capacity of 170 mAh g^{-1} can be maintained in up to 15 000 cycles after stabilization. The other two comparison samples, as previously analyzed, show a rapid decay and convergence of capacity. To further highlight the performance advantage in sodium-ion batteries, the cycling performance of NC@T/H–MoS_2@NPC at a current density of 2 A g^{-1} is demonstrated in Figure S22 (Supporting Information). A high specific capacity of 215 mAh g^{-1} can be stably provided after 1000 cycles. The performance advantages of NC@T/H–MoS_2@NPC in SIBs are also particularly evident in studies of the same type, as plotted in Figure 5k. The references and dates involved in the figure are listed in Table S5 (Supporting Information). In the capacity differential curve, NC@T/H–MoS_2@NPC (Figure 5l) exhibits significantly outstanding cycling reversibility at a current density of 0.5 A g^{-1} compared to the other two comparison samples (Figure S20a,b, Supporting Information). At the high current density of 5 A g^{-1}, the oxidized peaks can hardly show a similar left-shifted trend as that of LIB (Figure 5m), but a general right-shifted one. However, compared to the comparison samples (Figure S20c,d, Supporting Information), the movement of the oxidation peaks of NC@T/H–MoS_2@NPC is significantly slower, and still exhibits superior charge handling. In the EIS test (Figure S21b, Supporting Information), NC@T/H–MoS_2@NPC exhibits the smallest Rct, confirming the minimal charge transfer internal resistance. The calculated Log $D_{Average}$ using GITT results is proportional to the ion diffusion rate (Figure S19d–f, Supporting Information). Among them, NC@T/H–MoS_2@NPC has the highest sodium ion diffusion rate. The excellent electrochemical kinetics can be attributed to the fast ion migration channels generated at the heterojunction interface, yielding similar conclusions as in LIB.

In the CV curves at 0.1 mV s^{-1} (Figure 5n), the peaks at 1.04 and 0.46 V in the first loop of the discharge region correspond to the formation of the SEI film and the embedding of Na^+ in the MoS_2 interlayer.[43] Two pairs of classical redox peaks appear at 1.86/1.88 and 0.85/0.86 V in subsequent cycles.[44] The four b-values obtained after fitting the four peak currents (Figure S21c, Supporting Information) according to Equations 1 and 2 are 0.95, 0.85, 0.95, and 0.92 (Figure S21d, Supporting Information). Similar to the LIBs, they are all much closer to 1, indicating that it is dominated by the battery behavior. A fit for the pseudocapacitance contribution is calculated and reached 86% at 1 mV s^{-1} (Figure S21e, Supporting Information). The results at the other sweeping speeds are shown in the bar graphs (Figure S21f, Supporting Information), and it can be seen that the pseudocapacitive contribution is always dominant.

2.4. Mechanism Analysis

After the above tests of electrochemical properties, although the behavior of NC@T/H–MoS_2@NPC in LIBs and SIBs is similar, there are still some differences. Most notably, in the LIB at a high current density of 10 A g^{-1}, NC@T/H–MoS_2@NPC shows a capacity enhancement ≈500 to 800 cycles, which has been preliminarily discussed from the point of view of capacity differential curves in the electrochemical performance analysis section. The performance of NC@T/H–MoS_2@NPC induced by different PA additions in the 10 A g^{-1} (LIB) environment is tested in Figure S23a (Supporting Information). When the addition of phytic acid is 0.1 mL (I_{1T}/I_{2H} = 16.46), according to the previous structural analysis, the phenomenon of blocking is rare, and the vast majority of the linear polypyrrole could participate in the intercalation, thus eventually exhibiting the XRD spectral pattern of nearly all broad layers. When the addition amount is increased to 2 mL (I_{1T}/I_{2H} = 0.24), there is a significant blocking phenomenon with rare intercalation, thus showing almost no broad layer pattern. In the electrochemical performance, samples with the addition of 0.1 and 2 mL show a rapid capacity degradation (Figure S23a, Supporting Information). While at the addition of 0.2, 0.5, and 1 mL (10, 2.5, and 1.85 for I_{1T}/I_{2H}, respectively), the MoS_2 in the system is the hybrid phase, and a generalized capacity enhancement phenomenon is observed. Thus, it is argued that the hybrid phase is the key to realize this capacity enhancement. Among them, the sample with the addition amount of 0.5 mL has the fastest activation rate and the smoothest capacity, presenting the most excellent electrochemical performance. At this point, the relative ratio of 1T phase and 2H phase is 2.5, in which 1T phase as the subject and 2H phase as the guest can maximize the advantages of the heterogeneous structure. During the cycling test in SIB under 5 A g^{-1} (Figure S23b, Supporting Information), all samples exhibit varying degrees of capacity degradation, with NC@T/H–MoS_2@NPC-0.5 showing the least degradation and maintaining the highest capacity. The following mechanistic discussion still chooses the sample with the addition of 0.5 mL as a representative to be carried out.

Further assistance from ex situ XRD is needed to correlate microscopic phase changes with macroscopic electrochemical properties. Six points in the charging and discharging process of LIBs and SIBs are selected for ex situ XRD testing, respectively. In **Figure 6a**, the most noteworthy changes are the disappearance and reappearance of peaks located near 13.6°. Based on previous characterization results, this peak represents the small-spaced 2H-phase MoS_2. There is no change in the discharge to 1.94 V, the intensity becomes less when discharged to 1.10 V. By the time it is fully discharged to 0.01 V, the peak disappears completely, indicating a complete reaction. In Figure S24 (Supporting Information), MoS_2 at this point exhibits Raman spectral patterns closer to the 1T phase. During the charging process, the peak reappeared. And when charged to 3 V, the vibrational mode peaks of in-plane Mo–S (A_g^1) reappear, indicating that the MoS_2 in the system returns to the original hybrid phase state, which corresponds to the results shown by the ex situ XRD. Such a process not only proves the reversibility of the charging and discharging but also the involvement of the small-spaced 2H-phase MoS_2 in the storage of Li^+. As plotted in Figure 6b, the insertion of Li^+ can lead to the small-spaced MoS_2 to be broad layer and undergo the transition from the 2H phase to the 1T phase.[45] Therefore, the small-spaced peaks gradually disappear with the discharge process, while the large-spaced peaks are consistently present. This is also confirmed by HRTEM after full charging (Figure 6h),

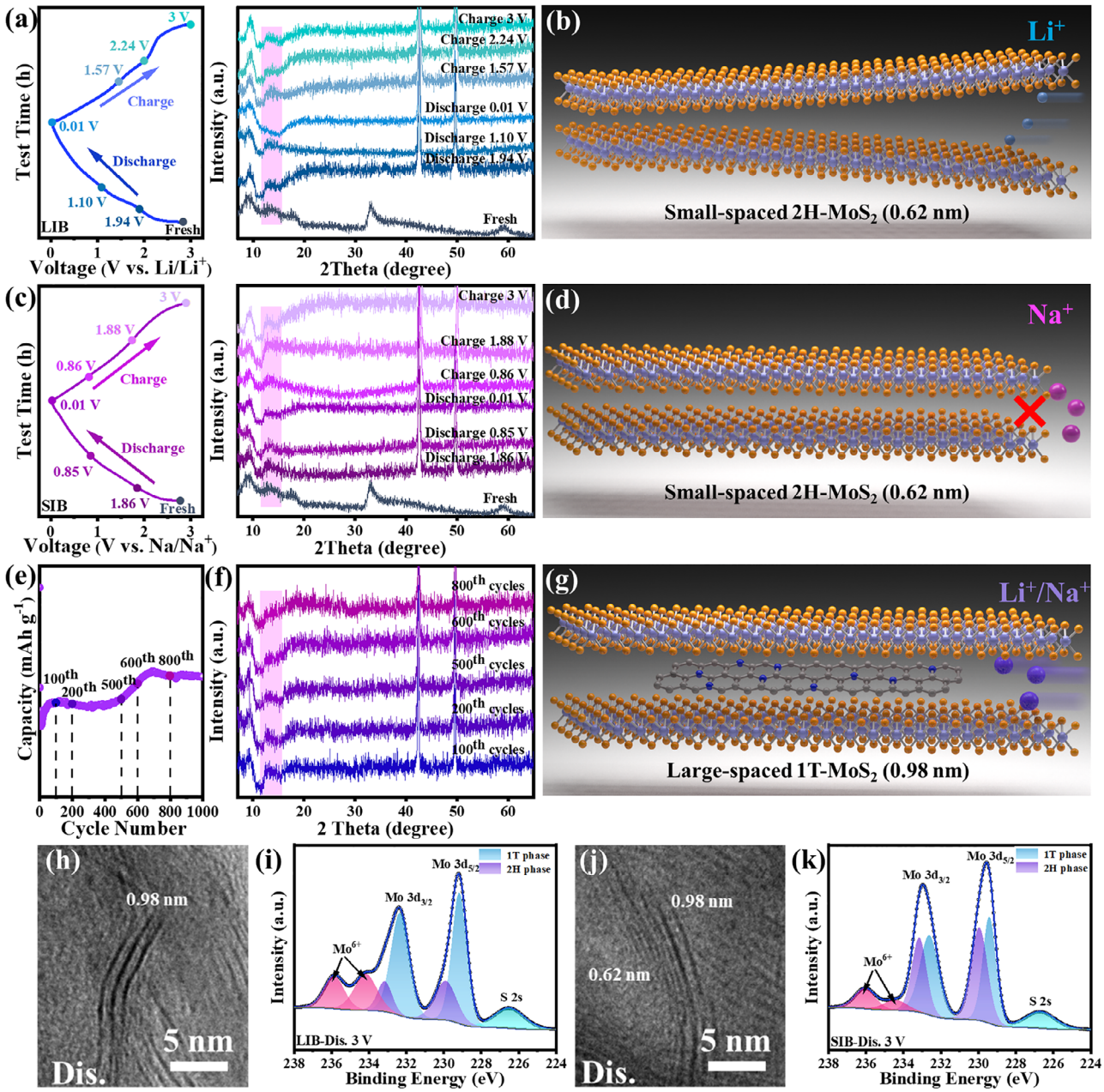

Figure 6. Ex situ XRD during charging and discharging of a) LIB and c) SIB; e) Cycling curve of NC@T/H–MoS_2@NPC for the first 1000 circles at 10 A g^{-1} in LIB; f) Ex situ XRD after different number of cycles in LIB (at 10 A g^{-1}). Conceptual diagram of small-spaced 2H-MoS_2 to store b) Li^+ or d) Na^+ and g) large-spaced 1T-MoS_2 to store Li^+/Na^+. HRTEM of electrode materials after fully discharge in h) LIB and j) SIB; Mo 3d XPS spectra of electrode materials after fully discharge in i) LIB and k) SIB.

where lattice fringes with small layer spacing disappear leaving only large layer spacing. At this time, the spectra of Mo 3d XPS deconvolution also changed considerably (Figure 6i), with a significant increase in the content of the 1T phase. It suggests that lithium ions activate part of the transition from 2H-phase MoS_2 to 1T-phase, which is in agreement with the results of the ex situ Raman spectrum. It should be noted that after electrochemical activation, the 1T-MoS_2 is easily oxidized, which also caused a significant enhancement of the intensity of the Mo^{6+} signal.[46] The SEM image after cycling is shown in Figure S25a (Supporting Information). The tubular structure is well maintained, and the flaky MoS_2 anchored to the tube can still be observed in the full-view TEM image (Figure S25b, Supporting Information). At this time, confirming the excellent structural stability of this tubular sandwich structure. After fully discharge, the region in Figure S25e (Supporting Information) is selected for the analysis of the scanning transmission electron microscopy (STEM) elemental mapping images (Figure S25f–h, Supporting Information), in which the Mo and S remain uniformly distributed. The results of the quantitative elemental analysis by energy dispersive X-ray

(EDX) spectroscopy are plotted in Figure S26a (Supporting Information). It should be noted that there is no signal of lithium in the quantitative analysis results, which is due to the extremely low energy of the excited Ka line of lithium making it difficult to be detected.

It is a different situation in Figure 6c, where the peak near 13.6° is always present. The pattern of in-plane Mo–S (A_g^1) is also consistently present in the spectrums after complete charging (SIB-Charge 3 V) and complete discharging (SIB-Discharge 0.01 V) in Figure S24 (Supporting Information). This is because the large radius of Na^+ makes it hard from inserting itself into the interlayers of the small-spaced 2H-phase MoS_2 (Figure 6d). In addition, the peaks located near 8° in both LIBs and SIBs are not significantly shifted during charging and discharging. This indicates that for large-spaced 1T-MoS_2, both Li^+ and Na^+ can insert and do not affect the crystal structure of MoS_2 (Figure 6g). Therefore, the coexistence of the two lattice stripes can still be observed in the HRTEM image after fully discharge (Figure 6j). Meanwhile, the relative proportion of the 1T and 2H phases in the Mo 3d XPS deconvolution does not change significantly (Figure 6k). The weak strengthening of the Mo^{6+} signal indicates that Na^+ has less electrochemical activation effect on this hybrid-phase MoS_2. In contrast, the constant insertion/deinsertion of Li^+ has a certain activating effect on the small-spaced 2H-phase MoS_2, which is reflected in the cycling performance as a result of the obvious activation observed in the LIBs with the increase of Li^+ flux (Figure 6e), but not in the SIBs. Five points are selected for ex situ XRD tests to study this activation process under the current density of 10 A g^{-1}, and the results are shown in Figure 6f. It can be observed that as the cycling proceeds, the small-spaced 2H-phase MoS_2 gradually decreases but is always present. Therefore, even though the intercalation behavior of Li^+ is highly reversible, its effect on MoS_2 interlayer extension becomes obvious with the increase of Li^+ flux, which ultimately leads to the permanent activation of some of the small-spaced 2H-phase MoS_2. Therefore, the capacity will be enhanced. But this part of MoS_2 is always present, ensuring the stability of the overall structure. For Na^+, as previously analyzed, it is hard to insert into the small-spaced 2H-phase MoS_2, and therefore this activation is not present in SIBs, regardless of the increase in Na^+ flux. But it is also the fact that the small-spaced 2H-phase MoS_2 is not involved in storing Na^+ that allows it to focus on playing the role in stabilizing the structure, thus giving SIBs exceptional cycling stability (15 000 cycles under 5 A g^{-1}). SEM (Figure S25c, Supporting Information) and TEM (Figure S25d, Supporting Information) full-view images of the electrode materials after cycling can be observed that the tubular sandwich and flaky structures remain intact, confirming the excellent stability of the nanostructures during sodium ion storage. After fully discharging, selecting the region in Figure S25i (Supporting Information) for STEM element mapping analysis, it is observed that the elements Mo and S remained uniformly distributed (Figure S25j–l, Supporting Information). The quantitative EDX quantification analysis (Figure S26b, Supporting Information) is able to detect the presence of the element Na, which is different from that in the LIBs.[47] The ex situ XRD patterns of NC@T–MoS_2@NC are recorded in Figure S27 (Supporting Information). The similar phenomenon can be observed that the peak near 13.6 ° is always present, even in the fully discharged state either for lithium or sodium ion storage process. Once again, it is verified that large-spaced 1T-MoS_2 has a good inclusion capacity for lithium/sodium ion intercalation and deintercalation.

The point to summarize is that no significant phase transition is observed in the ex situ XRD patterns. This appears to result from the fact that the broad layer treatment of MoS_2 using interlayer engineering shows more of the characteristics of a 2D layered material, i.e., intercalation behavior rather than a conventional transition metal sulfide transformation reaction. Similar conclusions have been reported in the literature.[19] This can avoid the problem of capacity loss caused by the dissolution of the intermediate products of the transformation reaction.

2.5. DFT Calculations

To elucidate the mechanism behind the exceptional performance of NC@T/H-MoS_2@NPC, density functional theory (DFT) calculations are employed. As discussed in Sections 2.1–2.4, the construction of 1T and 2H heterostructure plays a crucial role in the entire electrochemical process. Consequently, various microscopic models are constructed based on the actual interfaces present within NC@T/H–MoS_2@NPC, designated as 1T, 2H, 1T-2H, and 1T-NC, corresponding to the different phases of the interface (1T and 2H refer to 1T or 2H MoS_2, while NC represents the N-doped carbon layer). The Climbing Image Nudged Elastic Band (CINEB) method is used to simulate the diffusion of both Li and Na ions. Across the four interfaces, the ions exhibited similar energy trajectories (**Figure 7a,b**) and diffusion paths (Figure 7c), with bell-shaped curves observed during migration across the three types of MoS_2 interfaces. Lower energy barriers are found in the 2H and 1T-2H interfaces, likely due to ion migration between two octahedral voids via tetrahedral interstices, whereas linear migration from the bridging position is more prevalent in the 1T phase. The 1T-NC interface showed a distinctly different energy curve, with no significant energy barrier and a notable energy decline, suggesting advantages in both thermodynamics and kinetics. The introduction of the N-doped carbon layer not only provides a rapid ion diffusion path but also creates a potential well for ion storage, benefiting from the synergistic interaction between carbon and nitrogen. Carbon acts as a lubricant with minimal interaction with Li/Na ions, while nitrogen, supplying abundant electrons, forms a potential well for Li/Na ions. Additionally, the expansion effect due to the intercalation of carbon layers aids in ion diffusion on a larger scale.

The electronic structure analysis of different interfaces, shown in Figure 7d, reveals significant charge exchange and strong interaction between NC and 1T MoS_2. Charge density patterns, illustrated in Figure 7e, intuitively demonstrate the existence of a potential well, with electron accumulation increasing charge density around N atoms and trapping positive diffusion ions in the negative charge center. The improvement in electrochemical performance is not only due to the increased ion transport efficiency but also the accelerated electron transport. The density of states comparison between the two types of molybdenum disulfide,

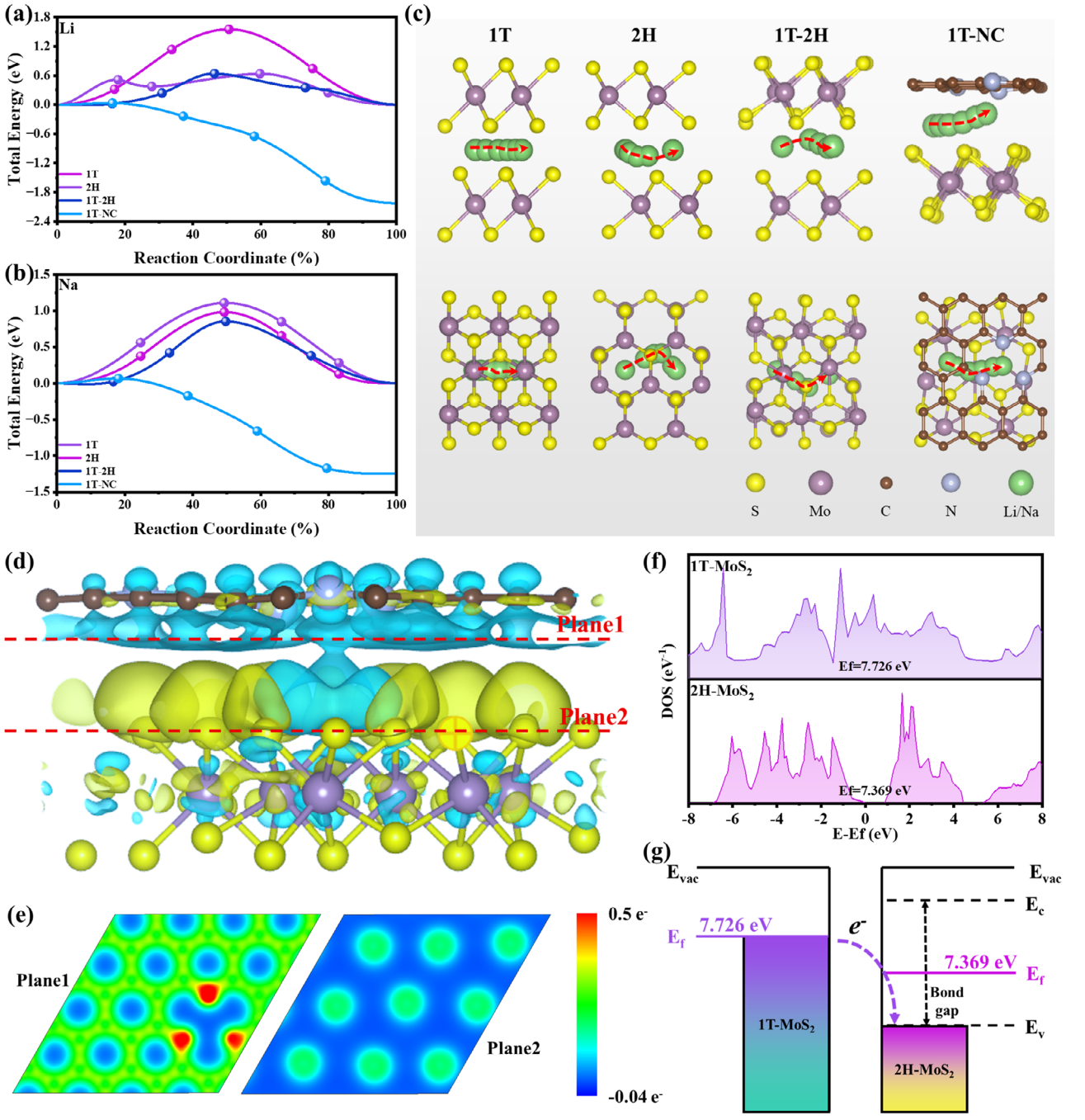

Figure 7. Energy profile for a) Li and b) Na diffusion in different matrices; c) Side and top views of Li/Na diffusion path in different matrices. d) Side view of charge density difference (CDD) of 1T-NC heterojunction (the charge accumulation and depletion of the CDD are denoted as yellow and blue with the isosurface of 9.97603e-05 e^-/ Å3 respectively.); e) 2D charge density patterns sliced from different (001) planes of heterojunction; f) Density of states (DOS) of 1T/2H MoS_2 and respective Fermi level energy; g) Schematic illustration of the formation mechanism and direction of electron transfer within the 1T- and 2H–MoS_2 heterostructure.

shown in Figure 7f, indicates that 1T MoS_2 is metallic without a bandgap, while 2H MoS_2 is semiconductive. The introduction of metallic 1T-MoS_2 inherently improves the overall electrical conductivity of the composite material (Figure S28, Supporting Information), and the Fermi level differences between the two phases create a built-in electric field that promotes charge and ion transport (Figure 7g). In summary, the outstanding electrochemical performance of NC@T/H–MoS_2@NPC is attributed to the modified interfaces that facilitate ion diffusion and storage, while the N-doped carbon layer and 1T/2H MoS_2 interfaces enhance ion transport efficiency and electronic conductivity through synergistic interactions and built-in electric fields.

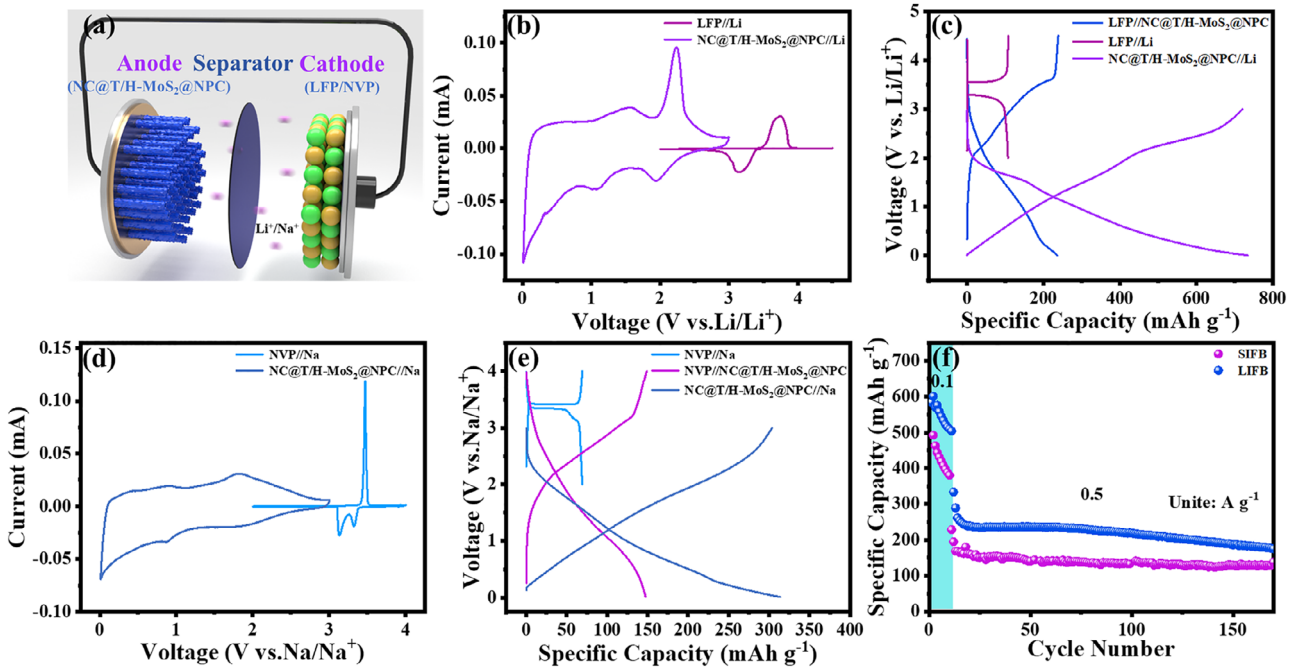

Figure 8. a) Schematic of full battery; CV curves at 0.1 mV s^{-1} sweep rate for b) LIB and d) SIB; GCD curves at 0.5 A g^{-1} current density for c) LIB/LIFB and e) SIB/SIFB; f) Cycling performance of the full battery at 0.5 A g^{-1} (The first ten circles are activated at 0.1 A g^{-1}).

2.6. Full Battery Performance

In view of the excellent performance in half batteries, $LiFePO_4$ (LFP)/$Na_3V_2(PO_4)_3$ (NVP) is used as cathode and NC@T/H–MoS_2@NPC as anode to assemble lithium-ion full batteries (LIFB)/sodium-ion full batteries (SIFB) to test their practical utilization value (**Figure** 8a). To find a suitable voltage test range, the CV curves of two electrode materials in the half-battery at the sweeping rate of 0.1 mV s^{-1} are plotted in Figure 8b. Among them, the curve of NC@T/H–MoS_2@NPC is consistent with the second circle in Figure 5g, and the test range is 0.01–3 V. For the half-battery of LFP, 2–4.5 V is chosen as the test interval. Therefore, in order to fully utilize the electrochemical activity of each component, the test range of LIFB is determined to be 0.01–4.5 V. Similarly, the test interval of SIFB is 0.01–4 V (Figure 8d). In the GCD curve (Figure 8c), the discharge curve of LFP//Li shows a clear plateau ≈3.6 V, which is consistent with the voltage position of the discharge peak of the CV curve. Correspondingly, a clear inflection point is observed near 3.6 V in the LFP//NC@T/H–MoS_2@NPC curve. This phenomenon proves that the full battery performance can be adequately optimized in the voltage range of 0.01–4.5 V with well-matched positive and negative electrode materials. Results are similar in the SIFB (Figure 8e). The CV curves of LIFB and SIFB at 0.1 mV s^{-1} are recorded in Figure S29 (Supporting Information), where the redox reactions of both positive and negative materials are fully exploited, confirming the good matching of voltage intervals. The rate performance of the full batteries at current densities from 0.1 to 5 A g^{-1} is tested in Figure S30a (Supporting Information), displaying satisfactory results. Both are able to possess close to 91% capacity retention with current densities back to 0.1 A g^{-1}. Finally, the cycling performance of SIFB and LIFB is tested at 0.5 A g^{-1} after 10 cycles of activation at 0.1 A g^{-1} (Figure 8f). The LIFB maintains a capacity of 175 mAh g^{-1} with the retention rate of 75% (vs 234 mAh g^{-1} on the 20th turn) after 170 cycles. Comparatively, the SIFB has a smoother curve but lower capacity, with a capacity of 126 mAh g^{-1} after 170 cycles and a retention rate of 80% (vs 158 mAh g^{-1} on the 20th turn). The LIFB and SIFB still possessed 75% and 73% capacity retention, respectively, after 300 cycles at a high current density of 1 A g^{-1} (Figure S30b, Supporting Information). The accelerated capacity fade observed in full-battery systems stems from three interconnected factors. First, unlike full-batteries with unlimited metal anode reserves, the fixed alkali metal inventory in full-batteries cannot compensate for irreversible losses through SEI formation, dead metal accumulation, and electrolyte decomposition.[48] Second, the wider operational voltage windows in full-battery promote electrolyte degradation at both electrodes, particularly through high-voltage oxidation processes that generate gaseous byproducts and resistive surface deposits.[49] Third, dynamic cross-talk between cathode and anode interfaces occurs through migrating species such as transition metal ions and polysulfides, establishing self-amplifying degradation cycles that increase interfacial resistance.[50] These coupled mechanisms collectively contribute to the more rapid performance decay observed in full-battery configurations compared to half-battery. After all, NC@T/H–MoS_2@NPC demonstrated stable performance in both LIFB and SIFB, confirming its potential for practical applications.

3. Conclusion

In summary, the organic molecule of phytic acid is utilized to block some MoS_2 end groups, inducing differential intercalation and polymerization of pyrrole monomers, thereby yielding

a 1T-2H MoS_2 heterostructure with distinct interlayer spacings (0.98 nm for 1T phase and 0.62 nm for 2H phase) upon annealing In addition, this heterogeneous structure is further integrated into a hierarchical sandwich architecture NC@T/H–MoS_2@NPC by anchoring onto NC nanotubes and encapsulating within NPC layers. The synergistic effect of the heterostructure and sandwich structures greatly improves the conductivity and stability of MoS_2. Thus, endowing NC@T/H–MoS_2@NPC with the ability to rapidly insert/de-insert Li^+/Na^+ at high current densities for the long term. The ex situ XRD characterizations clarify the insertion behavior of Li^+ and Na^+ and explain the reason for this fast-throughput ionic capability. The results of DFT calculations provide a theoretical basis for excellent electrochemical performance. Such idea of pre-partially blocking 2D material to achieve differential intercalation is inspiring for the construction of heterogeneous structures.

Supporting Information

Supporting Information is available from the Wiley Online Library or from the author.

Acknowledgements

This work was supported by the National Natural Science Foundation of China (52272296, 21601122, and 51502092), the Opening Project of the Jiangsu Key Laboratory for Chemistry of Low-Dimensional Materials (No. JSKC24026 and JSKC24028), Natural Science Research Projects for Higher Education Institutions in Jiangsu Province (24KJB430009), the Belt and Road Initiatives International Cooperation Project (20640770300), the Fundamental Research Funds for the Central Universities (JKD01211601 and 1222201718002), the National Overseas High-Level Talent Youth Program in China, and the Eastern Scholar Project of Shanghai.

Conflict of Interest

The authors declare no conflict of interest.

Data Availability Statement

The data that support the findings of this study are available from the corresponding author upon reasonable request.

Keywords

1T-2H heterostructure, differential intercalation, MoS_2, sandwich hierarchical structure

Received: October 10, 2025
Revised: November 1, 2025
Published online: November 12, 2025

[1] Z. Yang, H. Huang, F. Lin, *Adv. Energy Mater.* **2022**, *12*, 2200383.
[2] A. Masias, J. Marcicki, W. A. Paxton, *ACS Energy Lett.* **2021**, *6*, 621.
[3] S. Tian, W. Chen, R. Wang, C. Qin, Z. J. Jiang, Z. Jiang, *Adv. Funct. Mater.* **2024**, *34*, 2408035.
[4] F. Chen, C. Sun, S. J. Robertson, S. Chen, Y. Zhu, M. Shao, J. Wang, *Nano Energy* **2022**, *104*, 107894.
[5] C. Sun, M. Yang, T. Wang, Y. Shao, Y. Wu, X. Hao, *ACS Appl. Mater. Interfaces* **2017**, *9*, 26631.
[6] W. Liu, R. Huang, C. Yu, T. Xu, Y. Wang, H. Y. Yang, D. Yan, Y. Bai, *Adv. Funct. Mater.* **2025**, *35*, 2500352.
[7] M. Hariram, P. K. Pal, A. S. Chandran, M. R. Nair, M. Kumar, M. K. Ganesha, A. K. Singh, B. Dasgupta, S. Goel, T. Roy, P. W. Menezes, D. Sarkar, *Small* **2025**, *21*, 2410408.
[8] D. Voiry, R. Fullon, J. Yang, C. C. de Carvalho Castro e Silva, C. R. Kappera, I. Bozkurt, D. Kaplan, M. J. Lagos, P. E. Batson, G. Gupta, A. D. Mohite, L. Dong, D. Er, V. B. Shenoy, T. Asefa, M. Chhowalla, *Nat. Mater.* **2016**, *15*, 1003.
[9] Y. Tang, G. Li, S. Cui, W. Cui, H. Chong, L. Han, H. Pang, *Adv. Funct. Mater.* **2024**, *34*, 2403351.
[10] W. Wang, W. Zhang, R. Yu, F. Qiao, J. Wang, J. Wang, Q. An, *ACS Nano* **2024**, *18*, 35286.
[11] M. Hou, Y. Qiu, G. Yan, J. Wang, D. Zhan, X. Liu, J. Gao, L. Lai, *Nano Energy* **2019**, *62*, 299.
[12] M. Han, Y. Mu, J. Guo, L. Wei, L. Zeng, T. Zhao, *Nano-Micro Lett.* **2023**, *15*, 80.
[13] H. Peng, W. Miao, J. Zeng, Z. Wang, C. Yan, G. Ma, Z. Lei, *Adv. Sci.* **2025**, *12*, 2417288.
[14] S. Wang, D. Zhang, B. Li, C. Zhang, Z. Du, H. Yin, X. Bi, S. Yang, *Adv. Energy Mater.* **2018**, *8*, 1801345.
[15] S. J. R. Tan, S. Sarkar, X. Zhao, X. Luo, Y. Z. Luo, S. M. Poh, I. Abdelwahab, W. Zhou, T. Venkatesan, W. Chen, S. Y. Quek, K. P. Loh, *ACS Nano* **2018**, *12*, 5051.
[16] X. Wang, Q. Zheng, L. Wang, W. Jiang, *Adv. Funct. Mater.* **2025**, *35*, 2501720.
[17] T. Wang, M. Li, L. Qi, P. Jie, W. Yang, Y. Li, *Adv. Funct. Mater.* **2023**, *33*, 2308470.
[18] J. Qiu, F. Liu, S. Cheng, L. Zong, C. Zhu, C. Ling, A. Li, *ACS Sustainable Chem. Eng.* **2018**, *6*, 447.
[19] K. Liao, L. Chen, R. Meng, Y. Feng, S. Meng, H. Lu, J. Ma, C. Peng, C. Zhang, J. Yang, *J. Am. Chem. Soc.* **2024**, *146*, 12020.
[20] S. Wang, L. Zhao, J. Li, X. Tian, X. Wu, L. Feng, *J. Energy Chem.* **2022**, *66*, 483.
[21] L. Yu, X. Tao, D. Sun, L. Zhang, C. Wei, L. Han, Z. Sun, Q. Zhao, H. Jin, G. Zhu, *Adv. Funct. Mater.* **2024**, *34*, 2311471.
[22] J. Yang, M. Zhu, X. Duan, S. Wang, B. Yuan, M. Fu, *Appl. Catal. B-Environ.* **2021**, *297*, 120460.
[23] Y. Fang, J. Pan, J. He, R. Luo, D. Wang, X. Che, K. Bu, W. Zhao, P. Liu, G. Mu, H. Zhang, T. Lin, F. Huang, *Angew. Chem., Int. Ed.* **2018**, *57*, 1232.
[24] J. Li, J. Zhang, L. Yu, J. Gao, X. He, H. Liu, Y. Guo, G. Zhang, *Energy Storage Mater.* **2021**, *42*, 705.
[25] P. Chandra Lohani, A. Prasad Tiwari, A. Muthurasu, I. Pathak, M. Babu Poudel, K. Chhetri, B. Dahal, D. Acharya, T. H. Ko, H. Yong Kim, *Chem. Eng. J.* **2023**, *463*, 142280.
[26] W. Shen, C. Wang, Q. Xu, H. Liu, Y. Wang, *Adv. Energy Mater.* **2015**, *5*, 1400982.
[27] T. Wang, K. Yao, Y. Hua, E. G. Shankar, R. Shanthappa, J. S. Yu, *Chem. Eng. J.* **2023**, *457*, 141363.
[28] K. Chang, X. Hai, H. Pang, H. Zhang, L. Shi, G. Liu, H. Liu, G. Zhao, M. Li, J. Ye, *Adv. Mater.* **2016**, *28*, 10033.
[29] J. Ekspong, R. Sandström, L. P. Rajukumar, M. Terrones, T. Wågberg, E. Gracia-Espino, *Adv. Funct. Mater.* **2018**, *28*, 1802744.
[30] Y. Ren, M. Liang, Z. Zhou, X. Zhang, F. Yu, X. G. Li, J. Ma, *Adv. Funct. Mater.* **2025**, *35*, 2502601.
[31] H. Y. Lin, K. T. Le, P. H. Chen, J. M. Wu, *Appl. Catal. B-Environ.* **2022**, *317*, 121717.
[32] W. Li, M. Zhou, H. Li, K. Wang, S. Cheng, K. Jiang, *Energy Environ. Sci.* **2015**, *8*, 2916.

[33] G. Wang, X. Bi, H. Yue, R. Jin, Q. Wang, S. Gao, J. Lu, *Nano Energy* **2019**, *60*, 362.
[34] L. Chai, X. Wang, Y. Hu, X. Li, S. Huang, J. Pan, J. Qian, X. Sun, *Adv. Sci.* **2022**, *9*, 2105063.
[35] Y. Dong, Y. Liu, Y. Hu, K. Ma, H. Jiang, C. Li, *Sci. Bull.* **2020**, *65*, 1470.
[36] Y. Zhang, Z. Mu, C. Yang, Z. Xu, S. Zhang, X. Zhang, Y. Li, J. Lai, Z. Sun, Y. Yang, Y. Chao, C. Li, X. Ge, W. Yang, S. Guo, *Adv. Funct. Mater.* **2018**, *28*, 1707578.
[37] J. Sun, Z. Zhang, G. Lian, Y. Li, L. Jing, M. Zhao, D. Cui, Q. Wang, H. Yu, C. P. Wong, *ACS Nano* **2022**, *16*, 12425.
[38] J. Wu, J. Liu, J. Cui, S. Yao, M. Ihsan-Ul-Haq, N. Mubarak, E. Quattrocchi, F. Ciucci, J. K. Kim, *J. Mater. Chem. A* **2020**, *8*, 2114.
[39] Y. Xia, T. Yang, Z. Wang, T. Mao, Z. Hong, J. Han, D. L. Peng, G. Yue, *Adv. Funct. Mater.* **2023**, *33*, 2302830.
[40] G. Wang, J. Zhang, S. Yang, F. Wang, X. Zhuang, K. Müllen, X. Feng, *Adv. Energy Mater.* **2018**, *8*, 1702254.
[41] S. Xia, Y. Wang, Y. Liu, C. Wu, M. Wu, H. Zhang, *Chem. Eng. J.* **2018**, *332*, 431.
[42] L. Tang, B. Zhang, T. Peng, Z. He, C. Yan, J. Mao, K. Dai, X. Wu, J. Zheng, *Nano Energy* **2021**, *90*, 106568.
[43] H. Xie, B. Chen, C. Liu, G. Wu, S. Sui, E. Liu, G. Zhou, C. He, W. Hu, N. Zhao, *Energy Storage Mater.* **2023**, *60*, 102830.
[44] H. Wang, T. Yao, C. Li, L. Meng, Y. Cheng, *Chem. Eng. J.* **2020**, *397*, 125385.
[45] Z. Bo, X. Cheng, H. Yang, X. Guo, J. Yan, K. Cen, Z. Han, L. Dai, *Adv. Energy Mater.* **2022**, *12*, 2103394.
[46] S. Li, Y. Liu, X. Zhao, Q. Shen, W. Zhao, Q. Tan, N. Zhang, P. Li, L. Jiao, X. Qu, *Adv. Mater.* **2021**, *33*, 2007480.
[47] H. Xia, L. Zan, P. Yuan, G. Qu, H. Dong, Y. Wei, Y. Yu, Z. Wei, W. Yan, J. Hu, D. Deng, J. Zhang, *Angew. Chem., Int. Ed.* **2023**, *62*, 202218282.
[48] S. Oswald, M. Bock, H. A. Gasteiger, *J. Electrochem. Soc.* **2023**, *170*, 090505.
[49] C. Niu, H. Lee, S. Chen, Q. Li, J. Du, W. Xu, J. Zhang, M. Whittingham, J. Xiao, J. Liu, *Nat. Energy* **2019**, *4*, 551.
[50] A. M. Bates, Y. Preger, L. Torres-Castro, K. L. Harrison, S. J. Harris, J. Hewson, *Joule* **2022**, *6*, 742.